Improved Deadbeat Predictive Current Control of Dual Three-Phase Variable-Flux PMSM Drives With Composite Disturbance Observer

Kailiang Yu, *Student Member, IEEE*, and Zheng Wang, *Senior Member, IEEE*

***Abstract*—The dual three-phase variable-flux permanent-magnet synchronous motors (VF-PMSM) have received more attention in the variable-speed drive applications since they have advantages of high-efficiency in flux-tuning ability, low current stresses in phase legs and high fault-tolerant capability. The magnetization-state of the permanent magnets in VF-PMSM can be manipulated by the larger *d*-axis current pulse. However, the accompanied issues of parameter variation and inherent model uncertainty in magnetization manipulation of VF-PMSM increase the difficulty in parameter tuning for conventional proportional-integral controller, which deteriorates the control performance in current loop. To achieve the high performance of current tracking, an improved deadbeat predictive current control (DPCC) with composite disturbance observer has been proposed for dual three-phase VF-PMSM in this article. In the proposed composite disturbance observer, the generalized proportional–integral observer (GPIO) is employed for tracking the time-varying disturbance, and the sliding-mode observer is designed to reduce the settling time caused by the high-order GPIO for the improvement of the system dynamics. The analysis about the bandwidth-parameterized method has been presented for tuning the coefficients of the composite observer. The experimental results are presented to verify the validity of the proposed DPCC with composite disturbance observer for dual three-phase VF-PMSM drives under model uncertainty and different operating conditions.**

***Index Terms*—Deadbeat predictive current control, generalized proportional–integral observer (GPIO), sliding-mode observer (SMO), Variable-flux permanent-magnet synchronous motor (VF-PMSM).**

I. Introduction

DUE TO the merits on power factor, efficiency and power/torque density, permanent-magnet synchronous motors (PMSM) have been widely used in various variable-speed drive applications, such as servo control, electric vehicles, domestic appliances, and so on [1]. In order to expand the speed range, the negative *d*-axis current will be employed to weaken the air-gap flux under high-speed regions given the limited supplied voltage. However, the existing continuous *d*-axis current will bring some side-effects, such as the extra copper loss and the decrease of the efficiency into the drive system. In addition, the maximum *q*-axis current has to be reduced under the current limitation of the power inverter and electrical machine.

Compared with the conventional flux-weakening mode of PMSM, the variable-flux PMSM (VF-PMSM) provides another attractive solution to operate under different speed regions by regulating the magnetization-state of the low–coercive force permanent magnets [2], [3]. In usual, the magnets of VF-PMSM include the PM materials with low-coercive force, e.g., AlNiCo or SmCo, which also means that they are easily magnetized by excitation currents. Meanwhile, the VF-PMSM can maintain the magnetization-state even if the larger excitation currents were removed owing to its irreversible characteristics. Recently, the dual three-phase winding configuration has been incorporated with the VF-PMSM, which can reduce the current stresses on the semiconductor switches with large magnetization current pulses. Besides, the dual three-phase VF-PMSM can offer other advantages for magnetization regulation such as the mitigation of dc-link current ripple [4] and the rotor flux linkage estimation [5].

The amplitudes of magnetization currents vary up to several times of the rated current and the duration time of the current pulse is required as short as possible to limit additional copper losses. The performance of current control plays a key role in magnetization control for the dual three-phase VF-PMSM, because it determines the effect of magnetization regulation. As introduced in [6], an improved feed-forward current controller compensating voltage variations has been incorporated with the PI controller during the magnetization and demagnetization manipulations. As reported in [7], a structured neural network-based flux estimation has been proposed for the dead-beat torque control to overcome the coupling between the machine parameters. However, the offline finite-element analysis (FEA) is required in above methods for the lookup table of compensation voltages or the data samples of the structured neural network, which are dependent on the detailed geometric data of electrical machine and thus increase the complexity of the overall control system. To avoid FEA, the high-performance current controller

Manuscript received June 1, 2021; revised September 18, 2021 and December 1, 2021; accepted December 31, 2021. Date of publication January 7, 2022; date of current version March 24, 2022. This work was supported in part by the National Natural Science Foundation of China under Grant 52077034 and in part by the Aeronautical Science Foundation of China under Grant 20200019069001. Recommended for publication by Associate Editor Y. Mohamed. *(Corresponding author: Zheng Wang.)*

The authors are with the School of Electrical Engineering, Southeast University, Nanjing 210096, China (e-mail: 230198654@seu.edu.cn; zwang@eee.hku.hk).

Color versions of one or more figures in this article are available at https://doi.org/10.1109/TPEL.2022.3141375.

Digital Object Identifier 10.1109/TPEL.2022.3141375

will be investigated to improve the performance of magnetization manipulation for dual three-phase VF-PMSM drives.

Previously, intensive control strategies have been studied for the current control loop, e.g., hysteresis control [8], proportional-integral (PI) control [9], sliding-mode control (SMC) [10], and predictive current control (PCC) [11]–[13]. Although PI control, hysteresis control and SMC methods do not need accurate system model parameters, their dynamic performance is limited if one set of constant parameters are adopted, and the parameter tuning is complicated for satisfactory performance under different operation conditions. Among them, the PCC offers the potential for a more precise control structure and full-compatibility with digital-control platforms [11]. The PCC can be categorized into two types according to the existence of modulators: direct PCCs without the modulator; and indirect PCCs with the modulator. Compared to direct PCCs, the deadbeat PCC (DPCC) with the space vector modulation technique shows good features of the low distortion, the low current ripple and the constant switching frequency. Regarded as the high-gain proportional control, the system model-based DPCC needs to solve two practical issues: One is the inherent delay in the sample and algorithm calculation, which has been mitigated by the one-step forward prediction in time [12]. The other issue is the model uncertainty, e.g., the parameter mismatch and the unmodeled dynamics, which can result in the steady-state error, and even make the system unstable [13]. Actually, the issue of model uncertainty becomes more severe for dual three-phase VF-PMSM drives during magnetization manipulation, where the rotor flux linkage and the inductance change dynamically owing to the magnetization-state variation of permanent magnets.

At present, massive efforts have been devoted to improving the DPCC robustness, e.g., the Luenberger-type current observers [14], the online parameter identification [15], the parallel integral loop [16], and the disturbance observers [17]–[20]. Among the aforementioned methods, the disturbance observers, especially the sliding-mode observer (SMO), have shown good compensation performance by regarding the model uncertainty as the lumped disturbance term. In [17], an adaptive SMO has been proposed for stator current and disturbance based on a novel adaptive sliding-mode reaching law in the disturbance. In [18], the second-order SMO (supertwisting algorithm) is employed as feed-forward compensation to correct the steady-state current error. However, these SMO-based observers usually adopt high-order or adaptive algorithms for suppressing the inherent chattering problem, which increases the difficulty in parameter tuning for a satisfactory response. In addition, the disturbances in the aforementioned methods are assumed to vary slowly or be bounded, which is inappropriate for the time-varying disturbance. Then, the generalized proportional–integral observers (GPIO) are employed for dealing with the time-varying system parameters in the PCC scheme in [19]. Furthermore, a composite observer based on the SMO observer and the Luenberger observer is designed to predict the stator current of the next sampling period and compensate for the output voltage of the PCC in [20]. In the composite observer, the sign function of SMO is replaced by a hyperbolic tangent function for chattering suppression. Although the chattering issue of SMO can be solved easily, the performance of steady-state error still cannot satisfy the current tracking of the composite observer.

For dual three-phase VF-PMSM drives, the larger d-axis current pulse used for magnetization manipulation brings some challenges in tracking performance of the current controller. First, the parameters such as the rotor flux linkage and inductance are changed distinctively during the magnetization process. The tracking performance of the conventional DPCC will be deteriorated owing to its high dependence on the accuracy of the electrical machine parameters. Second, the inaccurate tracking of d-axis and q-axis current components will worsen the performance of magnetization current pulse.

Aiming at achieving the high performance of current tracking, an improved DPCC scheme is proposed for the dual three-phase VF-PMSM by designing the composite disturbance observer including the GPIO and SMO. Compared with the existing DPCC solutions, the main contributions and differences of the proposed method could be summarized as follows.

1) The proposed DPCC scheme with composite disturbance observer not only retains the superiority of GPIO with the available tracking ability of time-varying disturbance, but also inherits the advantages of SMO on the dynamic regulation for reducing the settling time of the high-order GPIO.
2) Compared with some complicated methods, e.g., the high-order or adaptive algorithm, the proposed method with hyperbolic tangent function can easily alleviate the chattering problem caused by the sign function of SMO. Meanwhile, the existence of steady-state error caused by a hyperbolic tangent function can be avoided by the combination with GPIO in the proposed method.
3) The proposed DPCC scheme with composite disturbance observer can achieve zero steady-state error and fast dynamics for current tracking of the dual three-phase variable-flux PMSM drive with model uncertainty and parameter variation. Therefore, it facilitates good control performance for magnetization manipulation of the dual three-phase variable-flux PMSM drive with large d-axis current pulses.

The rest of this article is organized as follows. First, the mathematical model and the magnetization manipulation principle of dual three-phase VF-PMSM are presented in Section II. Then, the conventional DPCC scheme and its parameter sensitivity are analyzed in Section III. To improve the current tracking performance for magnetization manipulation, an improved DPCC with the composite disturbance observer has been proposed for dual three-phase VF-PMSM drive in Section IV. In Section V, the experiments are given to verify the performance of the proposed method. Finally, Section VI concludes this article.

II. Magnetization Manipulation of Dual Three-Phase VF-PMSM Drives

A. Model of Dual Three-Phase VF-PMSM Drives

As shown in Fig. 1, the dual three-phase VF-PMSM is comprised of two sets of three-phase stator windings with a phase shift of 30° electrical angle, which are ABC windings and DEF

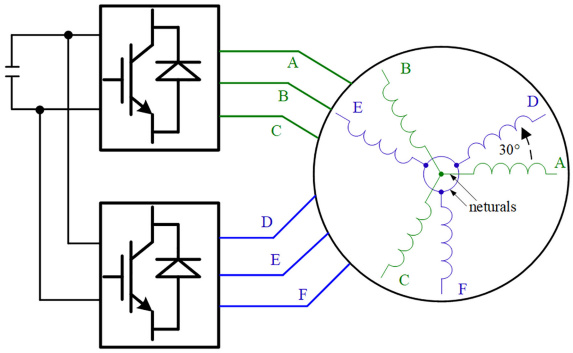

Fig. 1. System configuration of the dual three-phase VF-PMSM drives.

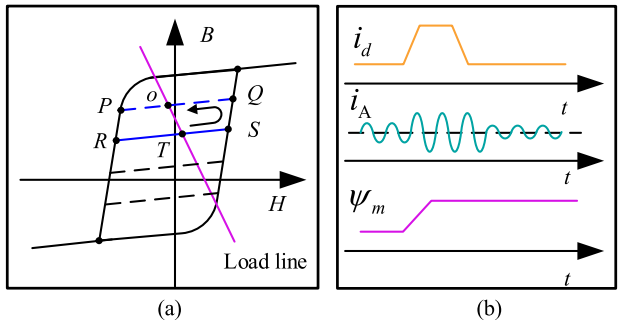

Fig. 2. Magnetization manipulation of VF-PMSM. (a) *B–H* curve of AlNiCo. (b) Schematic diagram of magnetization process.

windings, respectively. They are supplied by two sets of three-phase inverters with the common dc link. Neglecting the iron losses, the structural asymmetry, the magnetic saturation and the cross-coupling between d-axis and q-axis, the ideal model of dual three-phase VF-PMSM with isolated neutral points in the synchronous rotating frame can be obtained by vector space decomposition (VSD) as follows [4], [21]:

$$\begin{aligned} u_d &= R_s i_d + L_d \frac{di_d}{dt} + \frac{d\psi_m}{dt} - \omega L_q i_q \\ u_q &= R_s i_q + L_q \frac{di_q}{dt} + \omega(L_d i_d + \psi_m) \\ u_{z1} &= R_s i_{z1} + L_{\sigma s} \frac{di_{z1}}{dt} + \omega L_{\sigma s} i_{z2} \\ u_{z2} &= R_s i_{z2} + L_{\sigma s} \frac{di_{z2}}{dt} - \omega L_{\sigma s} i_{z1} \end{aligned} \tag{1}$$

where L_d and L_q are the d-axis inductance and q-axis inductance, respectively. R_s is the stator resistance and $L_{\sigma s}$ is the stator leakage inductance. ψ_m denotes the rotor flux linkage. u and i stand for the voltage and current, respectively. The subscripts "dq" and "z1z2" denote the dq reference frame and the z1z2 reference frame, respectively.

Based on the VSD theory, the space vectors of dual three-phase motor can be mapped into two orthogonal spaces: dq subspace (torque subspace) and z1z2 subspace (harmonic subspace). In this article, the magnetization control and torque regulation are related to the dq subspace. Since the control schemes of components on $z1z2$ subspace have been investigated intensively in the previous literature [22], the improved deadbeat PCC is focused on the dq subspace in this article.

Assuming that the sampling period T_s of the control system is small enough, the equivalent discretized form of (1) in the dq subspace using the zero-order hold method can be expressed as

$$\begin{bmatrix} i_d(k+1) \\ i_q(k+1) \end{bmatrix} = F(k) \begin{bmatrix} i_d(k) \\ i_q(k) \end{bmatrix} + G \begin{bmatrix} u_d(k) \\ u_q(k) \end{bmatrix} + M(k) \tag{2}$$

where

$$F(k) = \begin{bmatrix} 1 - \frac{R_s T_s}{L_d} & \omega(k) T_s \frac{L_q}{L_d} \\ -\omega(k) T_s \frac{L_d}{L_q} & 1 - \frac{R_s T_s}{L_q} \end{bmatrix}, G = \begin{bmatrix} \frac{T_s}{L_d} & 0 \\ 0 & \frac{T_s}{L_q} \end{bmatrix}$$

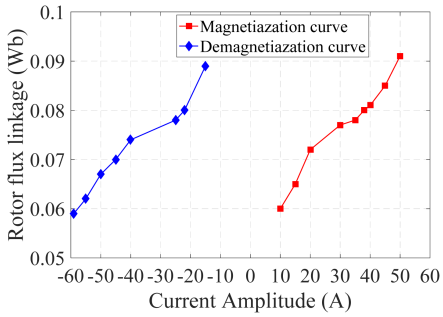

Fig. 3. Relationship between the rotor flux linkage and the amplitudes of magnetizing current.

$$M(k) = \begin{bmatrix} 0 \\ -\frac{\omega(k) T_s \psi_m(k)}{L_q} \end{bmatrix}. \tag{3}$$

B. Magnetization Manipulation of VF-PMSM Drives

As shown in Fig. 2(a), the hysteresis curves of the installed AlNiCo magnets are composed of the major loop and the minor loops. Different from the NdFeB magnets with the high coercive force, the AlNiCo magnets can be magnetized easily by the magnetomotive force (MMF) along the trajectory *TSQ* of Fig. 2(a). Owing to the irreversible characteristics of AlNiCo magnets, its new recoil line (*PQ*) will be determined by the initial point *Q* and the slope of the major loop once the magnetized/demagnetized MMF is disappeared. In addition, the working point will change from point *T* to point *O* according to the cross-point between the new recoil line *PQ* and the load line. Therefore, the VF-PMSM with AlNiCo magnets can be magnetized/demagnetized by the pulse form of current in armature windings instead of continuous current as shown in Fig. 2(b).

Fig. 3 gives the relationship between the rotor flux linkage and the amplitudes of the current pulse according to the experimental results. It indicates that the rotor flux linkage of VF-PMSM can be increased for magnetization by employing large positive magnetized current pulses. On the other hand, the rotor flux linkage can be reduced by using negative demagnetized current pulses. For the laboratory prototype of VF-PMSM in this article, the range of rotor flux linkage is from 0.57 to 0.9 Wb.

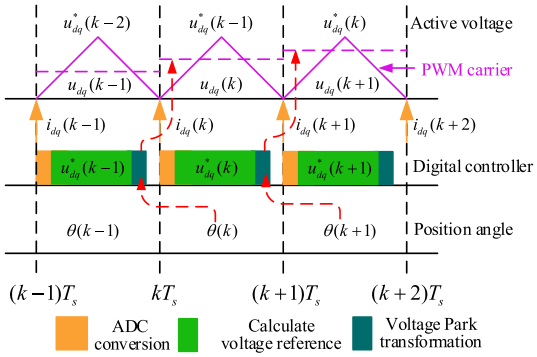

Fig. 4. Schematic diagram of control timing sequence in a digital system.

III. Conventional Deadbeat Current Control

A. Control Method

The nominal parameters or the estimated parameters of electrical machines are usually regarded as the given system parameters in digital controllers. Similar to (2), the discrete model of the dual three-phase VF-PMSM on dq subspace with given system parameters can be rewritten as

$$\begin{bmatrix} i_d(k+1) \\ i_q(k+1) \end{bmatrix} = \hat{F}(k) \begin{bmatrix} i_d(k) \\ i_q(k) \end{bmatrix} + \hat{G} \begin{bmatrix} u_d(k) \\ u_q(k) \end{bmatrix} + \hat{M}(k) \quad (4)$$

where the parameters of stator resistance, the rotor flux linkage, the d-axis and q-axis inductance in $\hat{F}(k)$, $\hat{G}$and $\hat{M}(k)$ are the given parameters in the controller, including $\hat{R}_s, \hat{\psi}_m, \hat{L}_d$, and $\hat{L}_q$.

Meanwhile, there exists the one-sampling-period delay between the reference voltage calculated at the instant of k and the actual one implemented at the instant of k+1 owing to the PMW implementation of the digital controller as shown in Fig. 4, which is modeled as

$$\begin{bmatrix} u_d^*(k) \\ u_q^*(k) \end{bmatrix} = \begin{bmatrix} u_d(k+1) \\ u_q(k+1) \end{bmatrix}. \quad (5)$$

Taking one-sample delay into consideration, the reference voltage at the instant of k should be determined by the states at the k+1 instant and k+2 instant, as given by

$$\begin{bmatrix} u_d^*(k) \\ u_q^*(k) \end{bmatrix} = \hat{G}^{-1} \left\{ \begin{bmatrix} i_d(k+2) \\ i_q(k+2) \end{bmatrix} - \hat{F} \begin{bmatrix} i_d(k+1) \\ i_q(k+1) \end{bmatrix} - \hat{M}(k+1) \right\}. \quad (6)$$

It should be noted that the current of $i_{dq}(k+1)$ has to be predicted through the discrete model at the k instant as follows:

$$\begin{bmatrix} \hat{i}_d(k+1) \\ \hat{i}_q(k+1) \end{bmatrix} = \hat{F}(k) \begin{bmatrix} i_d(k) \\ i_q(k) \end{bmatrix} + \hat{G} \begin{bmatrix} u_d^*(k-1) \\ u_q^*(k-1) \end{bmatrix} + \hat{M}(k). \quad (7)$$

Substituting (7) into (6) and considering the currents of $i_{dq}(k+2)$ as the reference current as i_{dq}^*, the DPCC with two-sample delays can be achieved by the appropriate voltage as

$$\begin{bmatrix} u_d^*(k) \\ u_q^*(k) \end{bmatrix} = \hat{G}^{-1} \left\{ \begin{bmatrix} i_d^*(k+2) \\ i_q^*(k+2) \end{bmatrix} - \hat{F} \begin{bmatrix} \hat{i}_d(k+1) \\ \hat{i}_q(k+1) \end{bmatrix} - \hat{M}(k+1) \right\}. \quad (8)$$

In addition, the reference voltages $u_{dq}^*(k)$ calculated at the k instant are implemented at the k+1 instant in the stationary frame. Hence, the difference of position angle for the field-oriented transformation at these two instants should be considered. In other words, the position angle of the reference voltage employed at the k instant should be compensated as follows:

$$u_{\alpha\beta}^*(k) = u_{dq}^*(k) e^{j(\theta_k + \theta_{delay})} = u_{dq}^*(k) e^{j(2.5\theta_k - 1.5\theta_{k-1})}. \quad (9)$$

B. Impacts of System Parameter Mismatch

According to the control law in (7) and (8), it can be concluded that the conventional DPCC highly relies on the accuracy of the model of the electrical machine. However, there exist inevitable differences between the given system parameters and the actual parameters, which usually leads to the steady-state error in current tracking. In order to figure out the relationship between the parameter mismatch and the steady-state error, the parameter sensitivity is analyzed for DPCC in this section.

Substituting the control voltages from the conventional DPCC in (8) into the real system model of (2), it yields

$$\begin{aligned} &\begin{bmatrix} i_d(k+2) \\ i_q(k+2) \end{bmatrix} \\ &= \begin{bmatrix} \hat{L}_d & 0 \\ 0 & \hat{L}_q \end{bmatrix} \begin{bmatrix} i_d^*(k+2)/L_d \\ i_q^*(k+2)/L_q \end{bmatrix} - \frac{\omega T_s}{L_q} \begin{bmatrix} 0 \\ \Delta\psi_m(k+1) \end{bmatrix} \\ &\quad + \begin{bmatrix} \Delta L_d - \Delta R_s T_s & \omega T_s \Delta L_q \\ -\omega T_s \Delta L_d & \Delta L_q - \Delta R_s T_s \end{bmatrix} \begin{bmatrix} i_d(k+1)/L_d \\ i_q(k+1)/L_q \end{bmatrix} \\ &\quad - \begin{bmatrix} \hat{L}_d - \hat{R}_s T_s & \omega T_s \hat{L}_q \\ -\omega T_s \hat{L}_d & \hat{L}_q - \hat{R}_s T_s \end{bmatrix} \begin{bmatrix} \tilde{i}_d(k+1)/L_d \\ \tilde{i}_q(k+1)/L_q \end{bmatrix} \end{aligned} \quad (10)$$

where Δ stands for the deviations between the actual system parameters and the given parameters, given as $\Delta F = F - \hat{F}$. The F can be R_s, L_d, L_q, and ψ_m. $\tilde{i}_d(k+1) = \hat{i}_d(k+1) - i_d(k+1)$ and $\tilde{i}_q(k+1) = \hat{i}_q(k+1) - i_q(k+1)$.

It is reasonable that the currents on the d-axis and q-axis at different instants can approximately be regarded as the identical value under the steady-state condition. Assuming that $i_{dq}(k+2)$ is equal to $i_{dq}(k+1)$, (10) can be simplified as follows:

$$\begin{aligned} &i_d(k+2) \\ &= \frac{\hat{L}_d}{\hat{L}_d + T_s \Delta R_s} i_d^*(k+2) - \frac{\hat{L}_d - T_s \hat{R}_s}{\hat{L}_d + T_s \Delta R_s} \tilde{i}_d(k+1) \\ &\quad + \frac{\omega T_s}{\hat{L}_d + T_s \Delta R_s} \left[\Delta L_q i_q(k+1) - \hat{L}_q \tilde{i}_q(k+1) \right] \\ &i_q(k+2) \\ &= \frac{\hat{L}_q}{\hat{L}_q + T_s \Delta R_s} i_q^*(k+2) - \frac{\omega T_s}{\hat{L}_q + T_s \Delta R_s} \Delta\psi_m(k+1) \end{aligned}$$

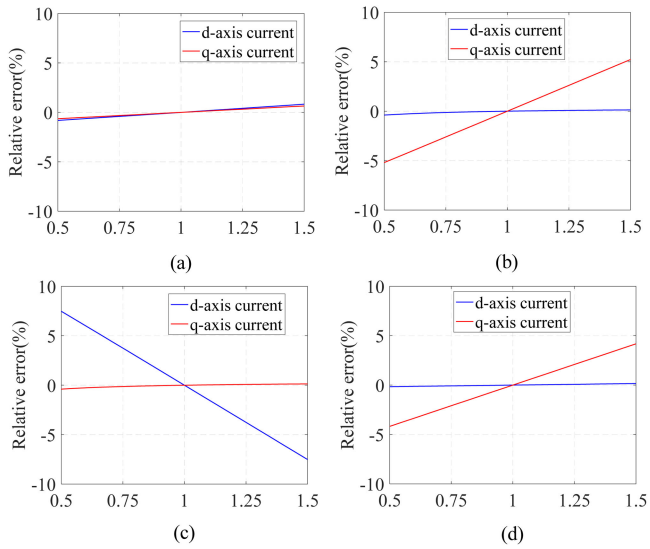

Fig. 5. Steady-state error of *dq*-axis currents with the conventional DPCC under the parameter mismatch. (a) Stator resistance mismatch. (b) *d*-axis inductance mismatch. (c) *q*-axis inductance mismatch. (d) Rotor flux linkage mismatch.

TABLE I
KEY PARAMETERS OF DUAL THREE-PHASE VF-PMSM

Parameter	Value	Parameter	Value
Pole pairs	4	Stator resistance (R_s)	0.4 Ω
Rated speed	750 r/min	*d*-axis inductance (L_d)	10 mH
Rated torque	8 N·m	*q*-axis inductance (L_q)	12 mH
Rated current	10 A	PM flux linkage (ψ_m)	from 0.06 Wb to 0.09 Wb

$$- \frac{\omega T_s}{\hat{L}_q + T_s \Delta R_s} \left[\Delta L_d i_d(k+1) - \hat{L}_d \tilde{i}_d(k+1) \right] - \frac{\hat{L}_q - T_s \hat{R}_s}{\hat{L}_q + T_s \Delta R_s} \tilde{i}_q(k+1). \tag{11}$$

Meanwhile, the prediction error at the k+1 instant under steady-state can be rewritten in (12) by substituting (2) into (7)

$$\begin{aligned} \tilde{i}_d(k+1) &= \frac{\Delta R_s T_s}{\hat{L}_d} i_d(k) - \omega \frac{\Delta L_q T_s}{\hat{L}_d} i_q(k) \\ \tilde{i}_q(k+1) &= \frac{\Delta R_s T_s}{\hat{L}_q} i_q(k) + \omega \frac{\Delta L_d T_s}{\hat{L}_q} i_d(k) + \frac{\omega T_s}{\hat{L}_q} \Delta \psi_m(k). \end{aligned} \tag{12}$$

From (11) and (12), the relationship between the current references and their responses using conventional DPCC is complicated under model parameter mismatch conditions. Fig. 5 shows the relative steady-state error in current tracking with DPCC under system parameter mismatch conditions. The parameters of the dual three-phase VF-PMSM are given in Table I. The operation speed is set as 750 r/min. And the reference value of *d*-axis current and *q*-axis current are set as 10 A. In Fig. 5, the relative errors of *dq*-axis currents are defined as $(i_d - i_{d\_\mathrm{ref}})/i_{d\_\mathrm{ref}} \cdot 100\%$ and $(i_q - i_{q\_\mathrm{ref}})/i_{q\_\mathrm{ref}} \cdot 100\%$.

As shown in Fig. 5(a), the parameter error of stator resistance has a limited effect on the steady-state error of *dq*-axis currents if the sampling time (200 μs) is small enough. Fig. 5(b) and (c) shows the steady-state errors of *dq*-axis currents under the parameter mismatch of L_d and L_q. For the steady-state error of *d*-axis current i_d, the parameter mismatch of *q*-axis inductance has more impacts than the parameter mismatch of *d*-axis inductance. On the contrary, the parameter mismatch of *d*-axis inductance has more impacts than the parameter mismatch of *q*-axis inductance for the steady-state error of *q*-axis current. Fig. 5(d) shows the impacts of parameter mismatch of rotor flux linkage. It indicates that the parameter mismatch of rotor flux linkage has more influence on the steady-state error of i_q, while has limited impacts on the steady-state error of i_d. It should be pointed out that the dynamics will also have impacts on the tracking ability of currents using the DPCC, which has not been considered in the models here.

IV. IMPROVED DEADBEAT CURRENT CONTROL WITH COMPOSITE DISTURBANCE OBSERVER

A. Proposed Composite Disturbance Observer

The parameter mismatch and un-modeled dynamics can be regarded as the lumped disturbance. Hence, the dynamic current model of dual three-phase VF-PMSM can be expressed with given system parameters

$$\begin{aligned} \hat{L}_d \frac{di_d}{dt} &= u_d - \hat{R}_s i_d + \omega \hat{L}_q i_q - f_d \\ \hat{L}_q \frac{di_q}{dt} &= u_q - \hat{R}_s i_q - \omega(\hat{L}_d i_d + \hat{\psi}_m) - f_q \end{aligned} \tag{13}$$

where f_d and f_q stand for the *d*-axis and *q*-axis lumped disturbances, respectively, and they are given by

$$\begin{aligned} f_d &= \Delta R_s i_d + \Delta L_d \frac{di_d}{dt} - \omega \Delta L_q i_q - \frac{d\psi_m}{dt} + \Delta u_d + \xi_d \\ f_q &= \Delta R_s i_q + \Delta L_q \frac{di_q}{dt} + \omega(\Delta L_d i_d + \Delta \psi_m) + \Delta u_q + \xi_q \end{aligned} \tag{14}$$

where Δu_d and Δu_q are the *d*-axis and *q*-axis error voltages caused by the VSI nonlinearity, respectively, and ξ_d and ξ_q denote the *d*-axis and *q*-axis unmodeled dynamics, respectively.

Using complex vector $\boldsymbol{x} = [i_d \quad i_q]^T$ and $\boldsymbol{u} = [u_d \quad u_q - \omega\hat{\psi}_m]^T$, (13) can be rewritten as

$$\dot{\boldsymbol{x}} = \boldsymbol{A}\boldsymbol{x} + \boldsymbol{B}\boldsymbol{u} - \boldsymbol{B}\boldsymbol{f} \tag{15}$$

where

$$\boldsymbol{A} = \begin{bmatrix} -\hat{R}_s/\hat{L}_d & \omega\hat{L}_q/\hat{L}_d \\ -\omega\hat{L}_d/\hat{L}_q & -\hat{R}_s/\hat{L}_q \end{bmatrix}, \boldsymbol{B} = \begin{bmatrix} 1/\hat{L}_d & 0 \\ 0 & 1/\hat{L}_q \end{bmatrix}. \tag{16}$$

In order to eliminate the influence of parameter mismatch and un-modeled dynamics, a new composite disturbance observer is proposed including the GPIO and SMO as follows:

$$\begin{aligned} \dot{\hat{\boldsymbol{x}}} &= \boldsymbol{A}\hat{\boldsymbol{x}} + \boldsymbol{B}\boldsymbol{u} - \boldsymbol{B}\hat{\boldsymbol{f}} + \boldsymbol{U}_{SMO} - \beta_1(\hat{\boldsymbol{x}} - \boldsymbol{x}) \\ \dot{\boldsymbol{z}}_1 &= \boldsymbol{z}_2 + \beta_2 \boldsymbol{B}^{-1}(\hat{\boldsymbol{x}} - \boldsymbol{x}) \end{aligned}$$

$$\begin{aligned}\dot{\boldsymbol{z}}_2 &= \boldsymbol{z}_3 + \beta_3 \boldsymbol{B}^{-1}(\hat{\boldsymbol{x}} - \boldsymbol{x}) \\ &\vdots \\ \dot{\boldsymbol{z}}_m &= \beta_{m+1}\boldsymbol{B}^{-1}(\hat{\boldsymbol{x}} - \boldsymbol{x})\end{aligned} \tag{17}$$

where the $\boldsymbol{z}_m$ stands for (m-1)-order derivative of the estimated value of lumped disturbance, such as $\boldsymbol{z}_1 = \hat{\boldsymbol{f}}, \boldsymbol{z}_2 = \hat{\boldsymbol{f}}^{(1)}, \boldsymbol{z}_3 = \hat{\boldsymbol{f}}^{(2)}, \ldots, \boldsymbol{z}_m = \hat{\boldsymbol{f}}^{(m-1)}$. $\hat{\boldsymbol{x}}$ is the estimated vector of state variables, which is denoted by the d-axis and q-axis currents as $\boldsymbol{x} = [\hat{i}_d \ \hat{i}_q]^T$.

It is noteworthy in (17) that the $\boldsymbol{U}_{\rm SMO}$ stands for the SMC function and the coefficients of $\beta_{1,\ldots,m}$ are designed for tracking the time-varying disturbance according to the GPIO.

1) Structural Analysis of SMO: According to [23], the sliding surface can be selected as the error between the estimated and actual dq-axis currents

$$\boldsymbol{s} = \hat{\boldsymbol{x}} - \boldsymbol{x} = \begin{bmatrix} \tilde{i}_d \\ \tilde{i}_q \end{bmatrix} = \begin{bmatrix} \hat{i}_d - i_d \\ \hat{i}_q - i_q \end{bmatrix}. \tag{18}$$

In this article, the reaching law is selected as the constant plus proportional rate reaching law ($\dot{\boldsymbol{s}} = -\boldsymbol{Q}\mathrm{sgn}(\boldsymbol{s}) - \boldsymbol{K}\boldsymbol{s}$), where the $\boldsymbol{Q}\mathrm{sgn}(\boldsymbol{s})$ and $\boldsymbol{K}\boldsymbol{s}$stand for the constant rate reaching law and the proportional rate reaching law. In this article, the proportional coefficient of $\boldsymbol{K}\boldsymbol{s}$ is chosen as identical to the coefficient β_1 of the GPIO for the separation design of these two observers. Thus, the reaching law can be defined as

$$\dot{\boldsymbol{s}} \triangleq -\gamma \mathrm{sgn}(\boldsymbol{s}) - \beta_1 \boldsymbol{s}. \tag{19}$$

Subtracting (17) into (15) and substituting the result into the derivative of (18), it yields

$$\dot{\boldsymbol{s}} = \dot{\hat{\boldsymbol{x}}} - \dot{\boldsymbol{x}} = \boldsymbol{A}\boldsymbol{s} - \beta_1 \boldsymbol{s} - \boldsymbol{B}(\hat{\boldsymbol{f}} - \boldsymbol{f}) + \boldsymbol{U}_{\rm SMO}. \tag{20}$$

Considering $\boldsymbol{B}(\hat{\boldsymbol{f}} - \boldsymbol{f})$ as the disturbances, the control law of the SMO can be designed in (21) with (19) and (20)

$$\boldsymbol{U}_{\rm SMO} = -\boldsymbol{A}\boldsymbol{s} - \gamma \mathrm{sgn}(\boldsymbol{s}). \tag{21}$$

In order to suppress the chattering problem of high-frequency switching caused by the sign function, the sign function can be replaced with a hyperbolic tangent function $f(x) = \tan h(x)$. Hence, the control law of SMO can be rewritten as

$$\boldsymbol{U}_{\rm SMO} = -\boldsymbol{A}\boldsymbol{s} - \gamma \tan h(\boldsymbol{s}) = -\boldsymbol{A}\boldsymbol{s} - \gamma \frac{e^{j\boldsymbol{s}} - e^{-j\boldsymbol{s}}}{e^{j\boldsymbol{s}} + e^{-j\boldsymbol{s}}}. \tag{22}$$

2) Structural Analysis of GPIO: Before the analysis of GPIO, we can derive the error dynamic model of m-order derivative of the lumped disturbance. The estimated current error and the m-order error of derivative of the lumped disturbance can be expressed as

$$\begin{aligned}\boldsymbol{e}_1 &= \hat{i}_{dq} - i_{dq} \\ \boldsymbol{e}_2 &= \boldsymbol{z}_1 - \boldsymbol{f} \\ \boldsymbol{e}_3 &= \boldsymbol{z}_2 - \boldsymbol{f}^{(1)} \\ &\vdots \\ \boldsymbol{e}_{m+1} &= \boldsymbol{z}_m - \boldsymbol{f}^{(m-1)}.\end{aligned} \tag{23}$$

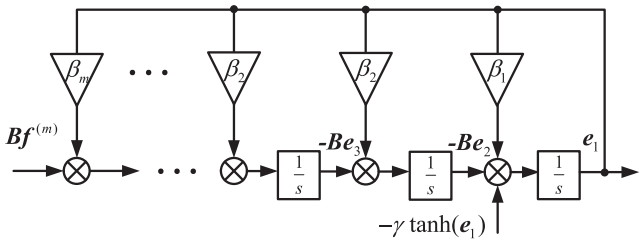

Fig. 6. Signal flowchart of error in the composite disturbance observer.

Taking the time derivative of (23) and combining with (15), (17) and (22), it yields

$$\begin{aligned}\dot{\boldsymbol{e}}_1 &= \dot{\boldsymbol{s}} = -\boldsymbol{B}\boldsymbol{e}_2 - \beta_1 \boldsymbol{e}_1 - \gamma \tan h(\boldsymbol{e}_1) \\ \dot{\boldsymbol{e}}_2 &= \boldsymbol{z}_2 - \boldsymbol{f}^{(1)} + \beta_2 \boldsymbol{e}_1 = \boldsymbol{e}_3 + \beta_2 \boldsymbol{B}^{-1}\boldsymbol{e}_1 \\ \dot{\boldsymbol{e}}_3 &= \boldsymbol{z}_3 - \boldsymbol{f}^{(2)} + \beta_3 \boldsymbol{e}_1 = \boldsymbol{e}_4 + \beta_3 \boldsymbol{B}^{-1}\boldsymbol{e}_1 \\ &\vdots \\ \dot{\boldsymbol{e}}_{m+1} &= \beta_{m+1}\boldsymbol{B}^{-1}\boldsymbol{e}_1 - \boldsymbol{f}^{(m)}.\end{aligned} \tag{24}$$

In order to illustrate (24) clearly, the dynamic error model using the matrix form can be rearranged as

$$\dot{\boldsymbol{E}} = \boldsymbol{A}\boldsymbol{E} + \boldsymbol{U} \tag{25}$$

where $\boldsymbol{E} = [\boldsymbol{e}_1 \ -\boldsymbol{B}\boldsymbol{e}_2 \ -\boldsymbol{B}\boldsymbol{e}_3 \ \cdots \ -\boldsymbol{B}\boldsymbol{e}_{m+1}]^T$

$$\boldsymbol{A} = \begin{bmatrix} -\beta_1 & 1 & 0 & \cdots & 0 \\ -\beta_2 & 0 & 1 & 0 & \vdots \\ -\beta_3 & 0 & 0 & 1 & 0 \\ \vdots & \vdots & \vdots & 0 & 1 \\ -\beta_{m+1} & 0 & \cdots & 0 & 0 \end{bmatrix}, \boldsymbol{U} = \begin{bmatrix} -\gamma \tan h(\boldsymbol{e}_1) \\ 0 \\ 0 \\ \vdots \\ \boldsymbol{B}\boldsymbol{f}^{(m)} \end{bmatrix}. \tag{26}$$

According to (25) and (26), the signal flowchart of error in the composite disturbance observer is presented in Fig. 6. And the transfer function from the m-order derivative of the lumped disturbance to the error of estimated dq-axis current can be derived as

$$\begin{aligned}H(s) &= \frac{1}{p(s)} \\ &= \frac{1}{s^{m+1} + \beta_1 s^m + \beta_2 s^{m-1} + \cdots + \beta_m s + \beta_{m+1}}.\end{aligned} \tag{27}$$

B. Design of Composite Disturbance Observer

The order of GPIO should be selected according to the type of the lumped disturbance. In addition, the maximum order of GPIO is limited by the level of system noise. That is to say, the m-order derivative of the estimated lumped disturbance should be zero, which can guarantee the zero-error of estimated dq-axis currents and disturbances according to (25) and (26). In this article, the magnetization current is chosen as the ramp type, which results that the lumped disturbance is also the ramp type as illustrated by (14). Hence, the order of GPIO is determined as 2 in this article for the disturbance with the ramp type

($f(t) = at + b$), which can be expressed as

$$\boldsymbol{f}^{(2)}(t) = (at+b)'' = 0. \tag{28}$$

On the other hand, it can be concluded from (27) that all poles of the transfer function H(s) can be arbitrarily placed on the Laplace plane (pole-zero map) by adjusting these coefficients $\beta_{1\cdots m} > 0$. Based on the bandwidth-parameterized method in [24], the polynomial coefficients of the n-th Butterworth low-pass filter is employed as

$$p(s) = \begin{cases} (s^2 + 2\xi\omega_n + \omega_n^2)^{(m+1)/2} & m = \text{odd} \\ (s+\omega_n)(s^2 + 2\xi\omega_n^2 + \omega_n^2)^{m/2} & m = \text{even}. \end{cases} \tag{29}$$

According to the polynomial coefficients of the second-Butterworth low-pass filter in (29), these coefficients $(\beta_1, \beta_2, \beta_3)$ can be rewritten as

$$\beta_1 = (2\xi+1)\omega_n, \beta_2 = (2\xi+1)\omega_n^2, \beta_3 = \omega_n^3 \tag{30}$$

where ξ and ω_n stand for the damping factor and the angular frequency, respectively. The overshoot is related to the damping factor, the range of which is from 0 to 1. It should be pointed out that the angular frequency is related to the poles and regarded as the absolute value of poles. In usual, the angular frequency is larger, and the dynamic performance is better. In this article, the damp factor ξ and the angular frequency ω_n are designed to be 0.707 and 500 rad/s, respectively.

In general, the gain of SMO should be greater than the disturbance of $\boldsymbol{B}(\hat{\boldsymbol{f}} - \boldsymbol{f})$, which can be derived as

$$\gamma \geq \left\| \boldsymbol{B}(\hat{\boldsymbol{f}} - \boldsymbol{f}) \right\|. \tag{31}$$

The convergence of disturbance has been guaranteed by the GPIO in this article. The parameter γ is employed to adjust the overshoot of the high-order GPIO. The parameter γ is larger, and the settling time is shorter. Hence, it can be adjusted by the trial and error according to the overshoot of current response.

C. Implementation of Improved DPCC With Composite Disturbance Observer

The aforementioned design and analysis about composite disturbance observer have been given in continuous time. For a digital controller, the discrete form of composite disturbance observer has to be implemented. There are many discrete methods to realize the transformation from the continuous domain to the discrete domain. Considering that the sampling time T_s of the control system is small (200 μs), the zero-order hold method is employed to discretize the integrators of the composite observer.

The integrator of the composite observer using zero-order hold method can be expressed as

$$D(z) = \mathcal{Z}\left(\frac{1-e^{-T_s s}}{s}\frac{1}{s}\right) = \frac{T_s}{z-1}. \tag{32}$$

Replacing the integrator in (17) by the discrete form of (32), and then combining with (22), the discrete form of the composite observer in d-axis and q-axis can be expressed as

$$\hat{i}_d(k+1) = (1 - \frac{\hat{R}_s T_s}{\hat{L}_d})i_d(k) + \omega T_s \frac{\hat{L}_q}{\hat{L}_d} i_q(k) + \frac{T_s}{\hat{L}_d}u_d(k) - \frac{T_s}{\hat{L}_d}\hat{f}_d(k) - \gamma \tan h(s_d)T_s - \beta_1\left[\hat{i}_d(k) - i_d(k)\right]T_s \tag{33a}$$

$$\hat{f}_d(k+1) = \hat{f}_d(k) + \hat{f}_d^{(1)}(k)T_s + \beta_2\left[\hat{i}_d(k) - i_d(k)\right]T_s\hat{L}_d$$

$$\hat{f}_d^{(1)}(k+1) = \hat{f}_d^{(1)}(k) + \beta_3\left[\hat{i}_d(k) - i_d(k)\right]T_s\hat{L}_d \tag{33b}$$

$$\hat{i}_q(k+1) = (1 - \frac{\hat{R}_s T_s}{\hat{L}_q})i_q(k) - \omega T_s \frac{\hat{L}_d}{\hat{L}_q} i_q(k) + \frac{T_s}{\hat{L}_q}u_q(k) - \frac{T_s}{\hat{L}_q}\hat{f}_q(k) - \gamma \tan h(s_q)T_s - \beta_1\left[\hat{i}_q(k) - i_q(k)\right]T_s \tag{34a}$$

$$\hat{f}_q(k+1) = \hat{f}_q(k) + \hat{f}_q^{(1)}(k)T_s + \beta_2\left[\hat{i}_q(k) - i_q(k)\right]T_s\hat{L}_q$$

$$\hat{f}_q^{(1)}(k+1) = \hat{f}_q^{(1)}(k) + \beta_3\left[\hat{i}_q(k) - i_q(k)\right]T_s\hat{L}_q. \tag{34b}$$

Then, the control voltages with the compensation of lumped disturbance at the k instant according to (8), which is derived as

$$\begin{bmatrix} u_d^*(k) \\ u_q^*(k) \end{bmatrix} = \hat{G}^{-1}\left\{ \begin{bmatrix} i_d^*(k+2) \\ i_q^*(k+2) \end{bmatrix} - \hat{F}\begin{bmatrix} \hat{i}_d(k+1) \\ \hat{i}_q(k+1) \end{bmatrix} - \hat{M}(k+1) + \begin{bmatrix} \hat{f}_d(k+1) \\ \hat{f}_q(k+1) \end{bmatrix} \right\}. \tag{35}$$

Based on the aforementioned analysis, the whole control scheme of the proposed DPCC with the composite disturbance observer can be illustrated in Fig. 7. The proposed DPCC with the composite disturbance can be divided into three parts: current prediction; disturbance observer; and deadbeat predictive current controller. The current prediction can integrate the SMO to obtain the current at the next sample instant with the aid of the estimated disturbance, which are expressed as (33a) and (34a). The current prediction with SMO can be regulated according to the error between the sampling current and model-based prediction current, which in turn leads to the fast dynamics of DPCC scheme. The GPIO can realize the estimation of time-varying high-order disturbance with (33b) and (34b). Finally, considering the one-sampling delay, the deadbeat predictive current controller can calculate the voltage reference through the predicted current $\hat{i}_{dq}(k+1)$ and the estimated disturbance $\hat{f}_{dq}(k+1)$.

V. Experimental Verification

A. Experimental Setup

Fig. 8 shows the experimental setup of the dual three-phase VF-PMSM drive. The detailed system parameters are the same as those in Table I of Section III. In the experiments, the dual three-phase VF-PMSM is mechanically coupled to a three-phase permanent-magnet synchronous generator (PMSG), supplying power for the resistive load. Thus, the load torque can be adjusted by changing resistive loads of PMSG. In the experimental setup, a Texas Instrument TMS320F28335 DSP is used to implement the control algorithm of the tested machine. The switching

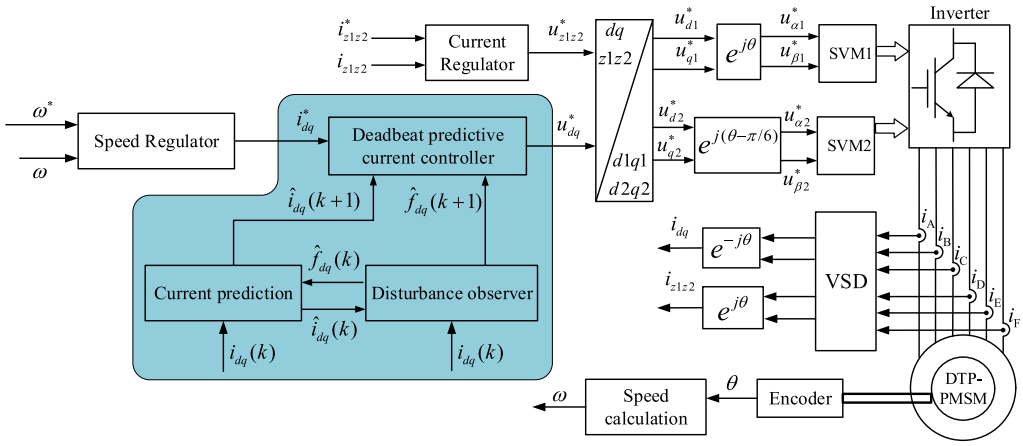

Fig. 7. Proposed deadbeat PCC scheme with the composite disturbance observer.

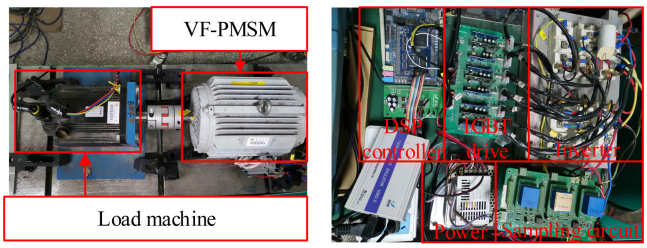

Fig. 8. Experimental setup. (a) Electrical machine. (b) Power circuits.

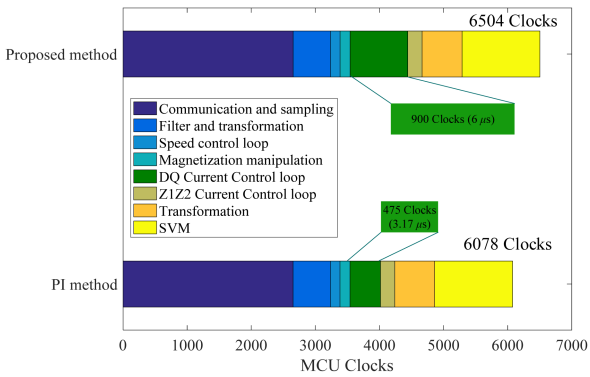

Fig. 9. Execution time of different control methods on MCU.

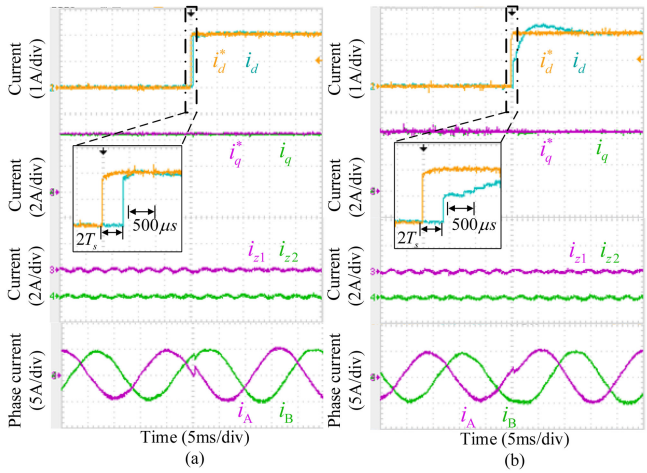

Fig. 10. Current response of the proposed DPCC with composite disturbance observer. (a) With accurate parameter ($\hat{R}_s = R_s$, $\hat{L}_d = L_d$, $\hat{L}_q = L_q$, $\hat{\psi}_m = \psi_m$). (b) With inaccurate parameter ($\hat{R}_s = 0.5R_s$, $\hat{L}_d = 0.5L_d$, $\hat{L}_q = 2L_q$, $\hat{\psi}_m = 0.75\psi_m$).

frequency of IGBT is 5 kHz and the sampling frequency is 5 kHz. In [25], the variation of inductance can be up to twice at different magnetization-states. In addition, the parameter mismatch would become more serious without the prior knowledge of machine parameters. Taking into account the extreme situation, the parameter mismatch of inductance is with the value of 400% in experiments of this article.

Fig. 9 shows the execution time of different control methods. The proposed method and the PI-based current control method are implemented in the microcontroller unit (MCU) of TMS320F28335, the main frequency of which is 150 MHz. The sampling period of this article is 200 μs, which is equal to 30 000 MCU Clocks. The main difference is the time consumed by the current control loop on *dq* subspace. For its execution time, the proposed DPCC method requires 900 Clocks and the PI method requires 475 clocks, which indicates that the execution time of *dq* current control loop has increased almost twice. The whole execution time of the proposed method and the PI method is 6504 clocks and 6078 clocks, respectively. It is obvious that both of the two methods can be executed in one sampling period. Therefore, the whole execution time of the proposed method is slightly increased compared to the PI-based current control method.

B. Performance of Proposed DPPC With Composite Disturbance Observer

In order to show the current tracking performance, the experimental results of the proposed improved DPCC have been presented with the accurate and inaccurate parameters, as shown in Fig. 10. The dual three-phase VF-PMSM drive operates under the rated speed of 750 r/min. The *q*-axis current reference is

determined by the output of the speed controller while the d-axis current reference can be set as zero for the simplicity of control.

As shown in Fig. 10(a), the amplitude of d-axis current reference abruptly steps from 0 to 2 A. As expected, the d-axis current can track the reference value with the two-sampling-period delay (400 μs) with accurate system parameters, which achieves the ideal current response of the DPCC. Fig. 10(b) shows the current tracking performance of the proposed DPCC with system parameter mismatch. It indicates that the proposed DPCC can still achieve zero steady-state tracking error in terms of the d-axis and q-axis current, although there exists a slight overshoot in the current response under parameter mismatch. In addition, it can be observed that the currents of z1z2 subspace are kept near zero with the proposed method, which confirms the aforementioned analysis that the control between the dq subspace and the z1z2 subspace are decoupled.

C. Comparison of the Conventional DPCC and Proposed DPCC

Since the system parameters such as the rotor flux linkage and the inductance change during magnetization manipulation of dual three-phase VF-PMSM drives, Fig. 11 compares the current tracking performance of the conventional DPCC and the proposed DPCC under variation of given system parameters. The dual three-phase VF-PMSM drive operates under the rated speed with the value of 600 r/min and the torque is 3.79 N·m.

Fig. 11(a) and (b) compares the steady-state dq-axis currents under the ramp variation of the rotor flux linkage. Due to the parameter sensitivity, the variation of rotor flux linkage will result in the steady-state error of q-axis current. As shown in Fig 11(a), the steady-state current error in q-axis has become 1.3 A with conventional DPCC when $\hat{\psi}_m$ is increased to $3\psi_m$. By contrast in Fig. 11(b), the tracking errors of d-axis and q-axis current maintain almost zero with the proposed DPCC under variation of rotor flux linkage. It indicates that the proposed DPCC has the better performance under the variation of the rotor flux linkage.

Similarly, Fig. 11(c) and (d) compare the current tracking performance under the ramp variation of q-axis inductance. From Fig. 11(c), the d-axis current error has expanded from 0 to 1 A using the conventional DPCC with the increase of the parameter mismatch of q-axis inductance. Moreover, the q-axis current appears the oscillations when the parameter mismatch $\Delta\hat{L}_q/L_q$ are greater than 100%. On the other hand, when the composited disturbance observer is employed, the proposed DPCC can maintain the good tracking performance during the whole variation process even $\Delta\hat{L}_q/L_q$ are 200% as demonstrated in Fig. 11(d).

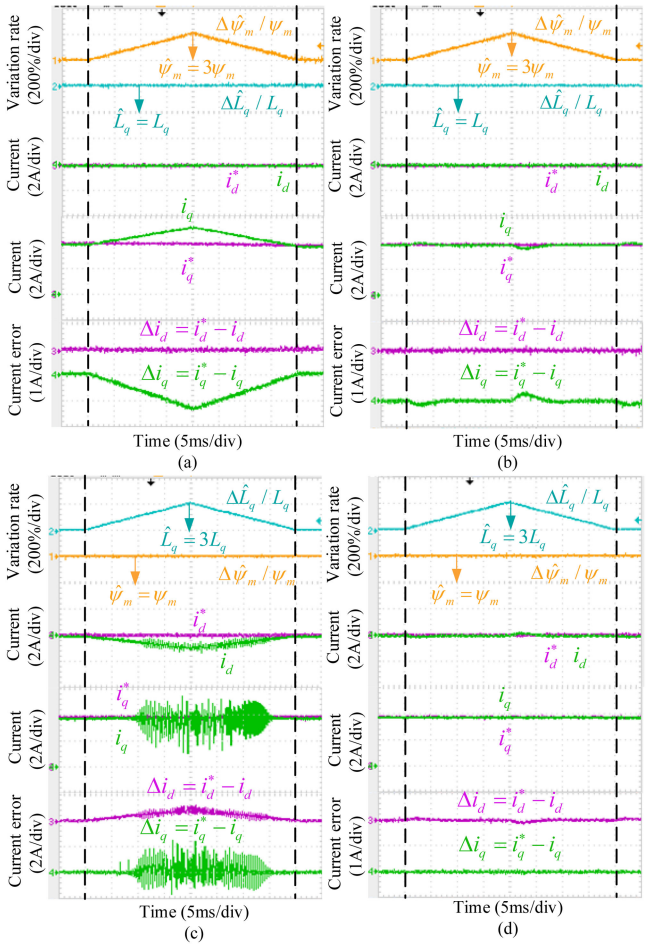

Fig. 11. Comparison of the conventional DPCC and proposed DPCC under parameter variation ($\hat{R}_s = R_s, \hat{L}_d = L_d, \hat{L}_q \in [L_q, 3L_q], \hat{\psi}_m \in [\psi_m, 3\psi_m]$). (a) Conventional DPCC with variation of rotor flux linkage. (b) Proposed DPCC with variation of rotor flux linkage. (c) Conventional DPCC with variation of the q-axis inductance. (d) Proposed DPCC with variation of the q-axis inductance.

D. Comparison of Different Composite Disturbance Observers

Fig. 12 shows the comparison results of composite disturbance observers with different orders. The speed of the dual three-phase VF-PMSM is 450 r/min and the torque is 4.59 N·m. The d-axis current reference is set as 4 A. Based on the parameter sensitivity in (11), the parameter mismatch of d-axis inductance ($\Delta\hat{L}_d/L_d$) from 0 to 3 will result in the steady-error on the q-axis current, even will cause unstable phenomena using the conventional DPCC.

Fig. 12(a) shows the performance of method A with the proposed DPCC, where the order of GPIO in the composite disturbance observer A is 1. Although the stability of current loop can be guaranteed, the steady-state error of q-axis current still exists with the value around 0.4 A. On the other hand, Fig. 12(b) shows the steady-state error of dq-axis current are almost kept zero with method B of the proposed method, where the order of GPIO in the composite disturbance observer is 2. In addition, it can be seen from the lumped disturbance voltages from these two methods that the method B with higher composite disturbance order has the better performance in tracking the time-varying disturbance. Hence, the order of GPIO is designed as 2 for the disturbance with the ramp type as illustrated in (28).

Figs. 13 and 14 compare the performance of DPCC with the proposed composite disturbance observer and three other disturbance observers. The speed of the dual three-phase VF-PMSM is 300 r/min. The other three disturbance observers are the SMO with the sign function, the SMO with the hyperbolic tangent

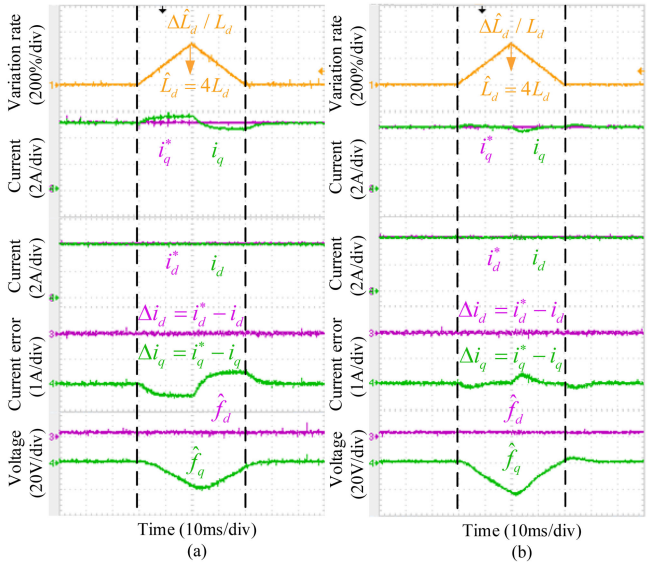

Fig. 12. Performance comparison of proposed DPCC methods with different orders of composite disturbance observers under the parameter variation of d-axis inductance ($\hat{R}_s = R_s, \hat{L}_d \in [L_d, 4L_d], \hat{L}_q = L_q, \hat{\psi}_m = \psi_m$). (a) Method A with the order of 1. (b) Method B with the order of 2.

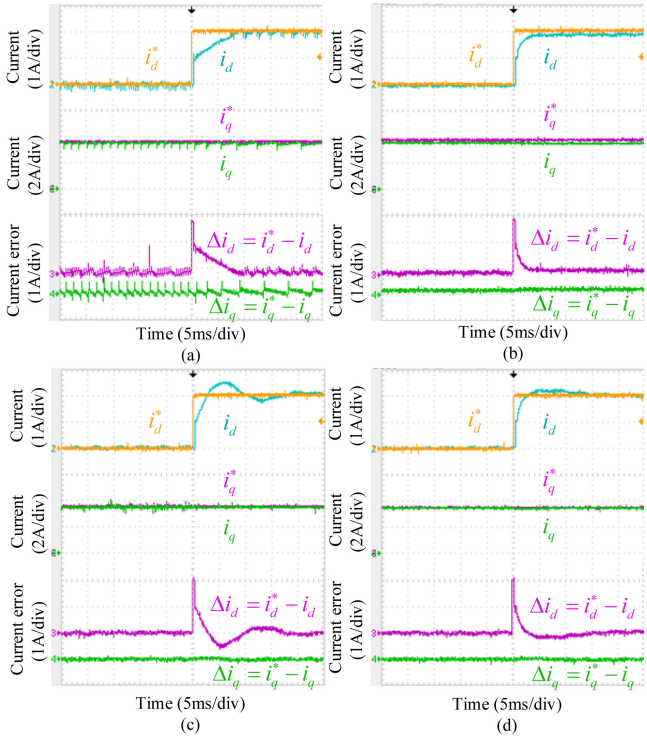

Fig. 13. Current error comparison of DPCC methods with different disturbance observers ($\hat{R}_s = 0.5R_s, \hat{L}_d = 0.5L_d, \hat{L}_q = L_q, \hat{\psi}_m = 0.75\psi_m$). (a) *Method* I: SMO with the sign function. (b) *Method* II: SMO with the hyperbolic tangent function. (c) *Method* III: GPIO. (d) *Method* IV: Proposed composite disturbance observer, including GPIO and SMO.

function, and the GPIO, where are termed as method I, method II, method III, respectively.

As shown in Figs. 13(a) and 14(a), the chattering phenomena can be found from the waveforms of the *dq*-axis currents and the *dq*-axis lumped disturbance voltages using SMO with the sign function, although the *dq*-axis currents can track their reference without the steady-state error. The gain of SMO in Method I is set as 500 ($\gamma = 500$). On the other hand, the SMO with the hyperbolic tangent function can alleviate the chattering problem, as shown in Figs. 13(b) and 14(b), where the larger gain of SMO ($\gamma = 2000$) is employed for method II. They indicate that the ripples of lumped disturbance voltages have been decreased from 14 to 0.8 V while the steady-state errors of *dq*-axis currents exist with the value of 0.2 A. Figs. 13(c) and 14(c) show the performance of DPCC using the GPIO with the order of 2. The damp factor and angular frequency of GPIO are 0.707 and 500 rad/s, respectively. It can be observed from the result of the method III that the overshoot is 0.6 A and the settling time is 17 ms. Figs. 13(d) and 14(d) show the measured performance using DPCC with the proposed composite disturbance observer. The coefficients setting of GPIO in the composite disturbance observer are identical to the method III, while the gain of SMO in composite disturbance observer is identical to the method II. It can be observed from Figs. 13(d) and 14(d) that the steady-state errors of *dq*-axis currents have reduced to zero and the ripples of *dq*-axis lumped disturbance voltages are within the acceptable range. Meanwhile, compared with Method III, the overshoot is reduced to 0.2 A, and settling time becomes 10 ms.

Based on the above comparisons, it can be concluded that the proposed DPCC method with composite disturbance observer has the better performance in terms of comprehensive performance in the steady-state errors, chattering problem, overshoot, and settling time.

E. Performance for Magnetization Manipulation

Finally, the proposed DPCC method is compared with the conventional PI controller in magnetization manipulation control for dual three-phase VF-PMSM, as shown in Fig. 15. The bandwidth of the conventional PI controller is designed as $2\pi \cdot 100$ rad/s while the damp factor, angular frequency and SMO gain of the composite disturbance observer are 0.707, 500 rad/s and 800 for the proposed DPCC, respectively. It should be noted that the PI controller does not include decoupling terms first considering that the inductance changes under different magnetization-states. Base on the relationship between the *d*-axis magnetization current and the rotor flux linkage in Fig. 3, the amplitude of *d*-axis magnetization current is chosen as 30 A for the increase of the rotor flux linkage to 0.078 Wb. During the magnetization process, the dual three-phase VF-PMSM operates by the speed control with the reference value of 450 r/min.

As shown in Fig. 15(a), the reference of *d*-axis current ramps from 0 A to 30 A within 12 ms, then maintains to be 30 A about 28 ms, and decreases from 30 to 0 A finally. After the magnetized current pulse, the estimated value of rotor flux linkage increases from 0.063 to 0.078 Wb. Hence, the steady-state value of *q*-axis current has decreased from 5.4 to 4.4 A owing to the increase of rotor flux linkage. During the magnetization process, the *q*-axis current is regulated by the speed control loop to mitigate the speed variation caused by the larger magnetization current. During the magnetization process, it is obvious that there exists

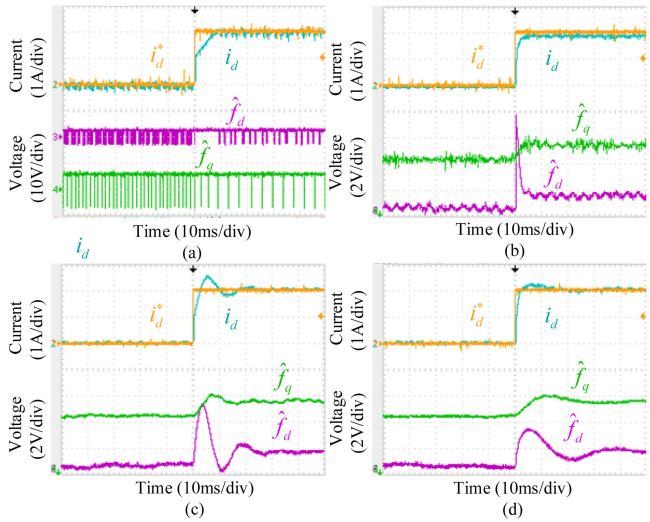

Fig. 14. Voltage comparison of DPCC methods with different disturbance observers ($\hat{R}_s = 0.5R_s, \hat{L}_d = 0.5L_d, \hat{L}_q = L_q, \hat{\psi}_d = 0.75\psi_d$). (a) *Method* I: SMO with the sign function. (b) *Method* II: SMO with the hyperbolic tangent function. (c) *Method* III: GPIO. (d) *Method* IV: Proposed composite disturbance observer, including GPIO and SMO.

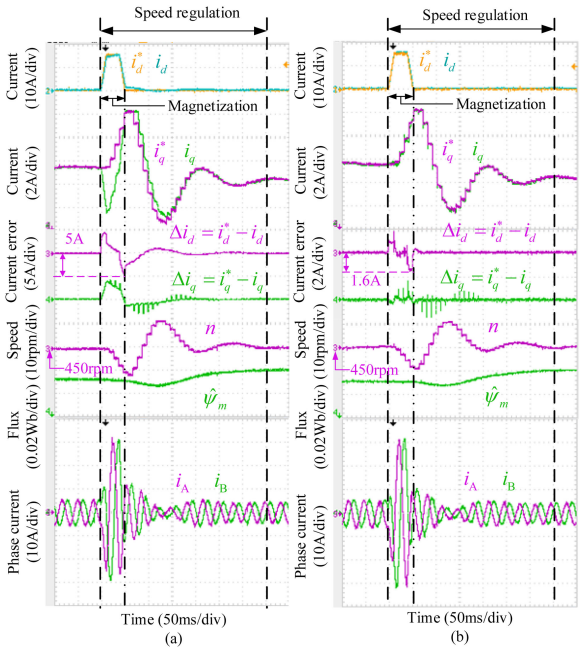

Fig. 15. Comparison of current tracking performance for magnetization manipulation. (a) Conventional PI controller without *dq*-axis decoupling. (b) Proposed DPCC with the composite disturbance observer.

a difference between the *dq*-axis current waveforms and their reference waveforms using the conventional PI controller. Owing to the larger amplitude of *d*-axis current and the parameter variation, the current loop with the conventional PI controller cannot achieve the good performance in current reference tracking. The maximum *d*-axis current error reaches 5 A. The relative error can be defined as the ratio between the maximum error of *d*-axis current and the reference value of *d*-axis current pulse. The relative error of conventional PI controller is 5/30 = 16.7%.

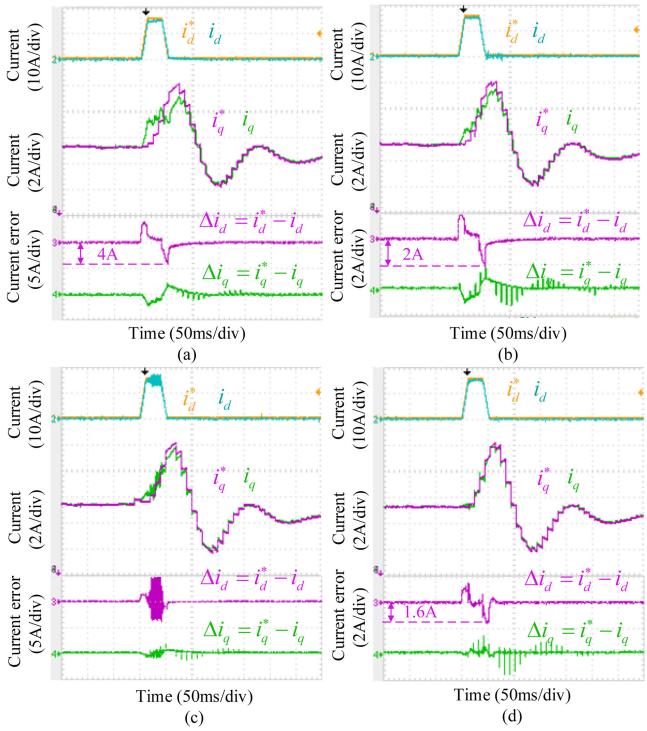

Fig. 16. Comparison of current tracking performance under different current control methods. (a) Conventional PI controller with bandwidth of 100 Hz. (b) Conventional PI controller with bandwidth of 200 Hz. (b) Conventional PI controller with bandwidth of 300 Hz. (d) Proposed DPCC with the composite disturbance observer.

On the other hand, the *d*-axis current can track their reference value well with the error less than 1.6 A, as shown in Fig. 15(b). Similarly, the relative error of the proposed method is only 1.6/30 = 5.3%.

Fig. 16 gives the comprehensive comparison experiments under different bandwidths of PI current controllers with *dq*-axis decoupling for the magnetization manipulation of dual three-phase VF-PMSM. From Fig. 16(a), the error of *d*-axis current using the conventional PI controller with the bandwidth of 100 Hz is 4 A, which is 13.3% of the reference of *d*-axis current pulses. With the *dq*-axis decoupling, the error of *q*-axis current has decreased to 2 A with the bandwidth of 100Hz. When the bandwidth increases to 200 Hz in Fig. 16(b), the error of *d*-axis current using PI controller can be further reduced to 2 A. When the bandwidth of PI controller is up to 300 Hz in Fig. 16(c), the oscillations appear in current waveforms. By comparison, the error of *d*-axis current using the proposed DPCC method is 1.6A, which is 5.3% of the reference of *d*-axis current pulses. It indicates the proposed DPCC method with composite disturbance observer can offer better performance in current tracking for magnetization manipulation of dual three-phase VF-PMSM.

VI. Conclusion

In this article, an improved DPCC method with composite disturbance observer has been proposed for dual three-phase VF-PMSM drives. Compared with the conventional DPCC, the proposed method can achieve the zero steady-state tracking error

and fast dynamics under parameter mismatch conditions. The proposed composite disturbance observer not only retains the superiority of GPIO in tracking time-varying disturbances but also inherits the advantages of SMO on the dynamic regulation for reducing the settling time brought by the high-order GPIO. The bandwidth-parameterized method has been employed for tuning the coefficients of the composite observer. The experimental results have demonstrated the better operation performance of the proposed improved DPCC for the dual three-phase VF-PMSM drives under the model uncertainty and the magnetization manipulation conditions.

REFERENCES

[1] E. Levi, F. Barrero, and M. J. Duran, "Multiphase machines and drives—Revisited," *IEEE Trans. Ind. Electron.,* vol. 63, no. 1, pp. 429–432, Jan. 2016.

[2] X. Zhu, L. Quan, D. Chen, M. Cheng, Z. Wang, and W. Li, "Design and analysis of a new flux memory doubly salient motor capable of online flux control," *IEEE Trans. Magn.*, vol. 47, no. 10, pp. 3220–3223, Oct. 2011.

[3] H. Yang, H. Lin, Z. Q. Zhu, D. Wang, S. Fang, and Y. Huang, "A variable-flux hybrid-PM switched-flux memory machine for EV/HEV applications," *IEEE Trans. Ind. Appl.*, vol. 52, no. 3, pp. 2203–2214, May/Jun. 2011.

[4] Z. Wang, X. Wang, X. Yang, C. Wen, Y. Gong, and Y. Hu, "Mitigation of DC-link current ripple for dual three-phase flux-adjustable hybrid PMAC drives using collaborative switching strategy," *IEEE Trans. Ind. Electron.*, vol. 67, no. 9, pp. 7202–7216, Sep. 2020.

[5] K. Yu, Z. Wang, X. Wang, and Z. Zou, "A simple online flux estimation for dual three-phase SPMSM drives using position-offset injection," *IEEE Trans. Power Electron.*, vol. 36, no. 10, pp. 11606–11617, Oct. 2021.

[6] J. Chen, J. Li, and R. Qu, "Analysis, modeling, and current trajectory control of magnetization state manipulation in variable-flux permanent magnet machines," *IEEE Trans. Ind. Electron.*, vol. 66, no. 7, pp. 5133–5143, Jul. 2019.

[7] A. Athavale, D. J. Erato, and R. D. Lorenz, "Enabling driving cycle loss reduction in variable flux PMSMs via closed-loop magnetization state control," *IEEE Trans. Ind. Appl.,* vol. 54, no. 4, pp. 3350–3359, Jul./Aug. 2018.

[8] M. J. Navardi, J. Milimonfared, and H. A. Talebi, "Torque and flux ripples minimization of permanent magnet synchronous motor by a predictive-based hybrid direct torque control," *IEEE J. Emerg. Sel. Topics Power Electron.,* vol. 6, no. 4, pp. 1662–1670, Dec. 2018..

[9] L. Harnefors and H.P. Nee, "Model-based current control of AC machines using the internal model control method," *IEEE Trans. Ind. Appl.,* vol. 34, no. 1, pp. 133–141, Jan./Feb. 1998..

[10] V. Repecho, D. Biel, and A. Arias, "Fixed switching period discrete-time sliding mode current control of a PMSM," *IEEE Trans. Ind. Electron.,* vol. 65, no. 3, pp. 2039–2048, Mar. 2018.

[11] Y. A. I. Mohamed and E. F. El-Saadany, "Robust high bandwidth discrete-time predictive current control with predictive internal model—A unified approach for voltage-source PWM converters," *IEEE Trans. Power Electron.*, vol. 23, no. 1, pp. 126–136, Jan. 2008.

[12] P. Cortes, J. Rodriguez, C. Silva, and A. Flores, "Delay compensation in model predictive current control of a three-phase inverter," *IEEE Trans. Ind. Electron.*, vol. 59, no. 2, pp. 1323–1325, Feb. 2012.

[13] R. Yang, L. Li, M. Wang, and C. Zhang, "Force ripple compensation and robust predictive current control of PMLSM using augmented generalized proportional–integral observer," *IEEE Trans. Emerg. Sel. Topics Power Electron.,* vol. 9, no. 1, pp. 302–315, Feb. 2021.

[14] J. C. Moreno, J. M. Espi Huerta, R. G. Gil, and S. A. Gonzalez, "A robust predictive current control for three-phase grid-connected inverters," *IEEE Trans. Ind. Electron.,* vol. 56, no. 6, pp. 1993–2004, Jun. 2009.

[15] Y. Yao, Y. Huang, F. Peng, J. Dong, and H. Zhang, "An improved deadbeat predictive current control with online parameter identification for surface-mounted PMSMs," *IEEE Trans. Ind. Electron.*, vol. 67, no. 12, pp. 10145–10155, Dec. 2020.

[16] H. Le-Huy, K. Slimani, and P. Viarouge, "Analysis and implementation of a real-time predictive current controller for permanent-magnet synchronous servo drives," *IEEE Trans. Ind. Electron.,* vol. 41, no. 1, pp. 110–117, Feb. 1994.

[17] X. Zhang, B. Hou, and Y. Mei, "Deadbeat predictive current control of permanent-magnet synchronous motors with stator current and disturbance observer," *IEEE Trans. Power Electron.*, vol. 32, no. 5, pp. 3818–3834, May 2017.

[18] B. Wang, Z. Dong, Y. Yu, G. Wang, and D. Xu, "Static-errorless deadbeat predictive current control using second-order sliding-mode disturbance observer for induction machine drives," *IEEE Trans. Power Electron.*, vol. 33, no. 3, pp. 2395–2403, Mar. 2018.

[19] J. Wang, F. Wang, G. Wang, S. Li, and L. Yu, "Generalized proportional integral observer based robust finite control set predictive current control for induction motor systems with time-varying disturbances," *IEEE Trans. Ind. Informat.*, vol. 14, no. 9, pp. 4159–4168, Sep. 2018.

[20] C. Zhang *et al.*, "Robust fault-tolerant predictive current control for permanent magnet synchronous motors considering demagnetization fault," *IEEE Trans. Ind. Electron.*, vol. 65, no. 7, pp. 5324–5334, Jul. 2018.

[21] Y. Zhao and T. A. Lipo, "Space vector PWM control of dual three-phase induction machine using vector space decomposition," *IEEE Trans. Ind. Appl.,* vol. 31, no. 5, pp. 1100–1109, Sep./Oct. 1995.

[22] Y. Hu, Z. Zhu, and K. Liu, "Current control for dual three-phase permanent magnet synchronous motors accounting for current unbalance and harmonics," *IEEE J. Emerg. Sel. Topics Power Electron.,* vol. 2, no. 2, pp. 272–284, Jun. 2014.

[23] W. Gao and J. C. Hung, "Variable structure control of nonlinear systems: A new approach," *IEEE Trans. Ind. Electron.*, vol. 40, no. 1, pp. 45–55, Feb. 1993.

[24] Y. C. Kim, L. H. Keel, and S. P. Bhattacharyya, "Transient response control via characteristic ratio assignment," *IEEE Trans. Autom. Control*, vol. 48, no. 12, pp. 2238–2244, Dec. 2003.

[25] J. Chen, J. Li, and R. Qu, "Maximum-torque-per-ampere and magnetization-state control of a variable-flux permanent magnet machine," *IEEE Trans. Ind. Electron.,* vol. 65, no. 2, pp. 1158–1169, Feb. 2018.

Kailiang Yu (Student Member, IEEE) received the B.E. degree from the School of Electrical Engineering, Southeast University, Nanjing, China, in 2016, and the M.S. degree from the School of Electrical Engineering, Huazhong University of Science and Technology, Wuhan, China, in 2019, both in electrical engineering. He is currently working toward the Ph.D. degree with the School of Electrical Engineering, Southeast University, Nanjing, China.

His research interests include the control of multiphase permanent magnet synchronous motor and parameter estimation.

Zheng Wang (Senior Member, IEEE) received the B.Eng. and M.Eng. degrees from Southeast University, Nanjing, China, in 2000 and 2003, respectively, and the Ph.D. degree from The University of Hong Kong, Hong Kong, in 2008.

From 2008 to 2009, he was a Postdoctoral Fellow with Ryerson University, Toronto, ON, Canada. He is currently a Full Professor with the School of Electrical Engineering, Southeast University, China. In these fields, he has authored more than 100 internationally refereed papers, 1 English book by IEEE-Wiley Press, and 2 English book chapters. His research interests include electric drives, power electronics, and renewable power generation.

Dr. Wang was the receipint of IEEE PES Chapter Outstanding Engineer Award, Outstanding Young Scholar Award of Jiangsu Natural Science Foundation of China, and several paper awards of journals and conferences. He is currently an Associate Editor for the IEEE TRANSACTIONS ON INDUSTRIAL ELECTRONICS and *Journal of Power Electronics.*